Volume 10
Number 10
14 March 2022
Pages 3613–3992

Journal of Materials Chemistry C

Materials for optical, magnetic and electronic devices

rsc.li/materials-c

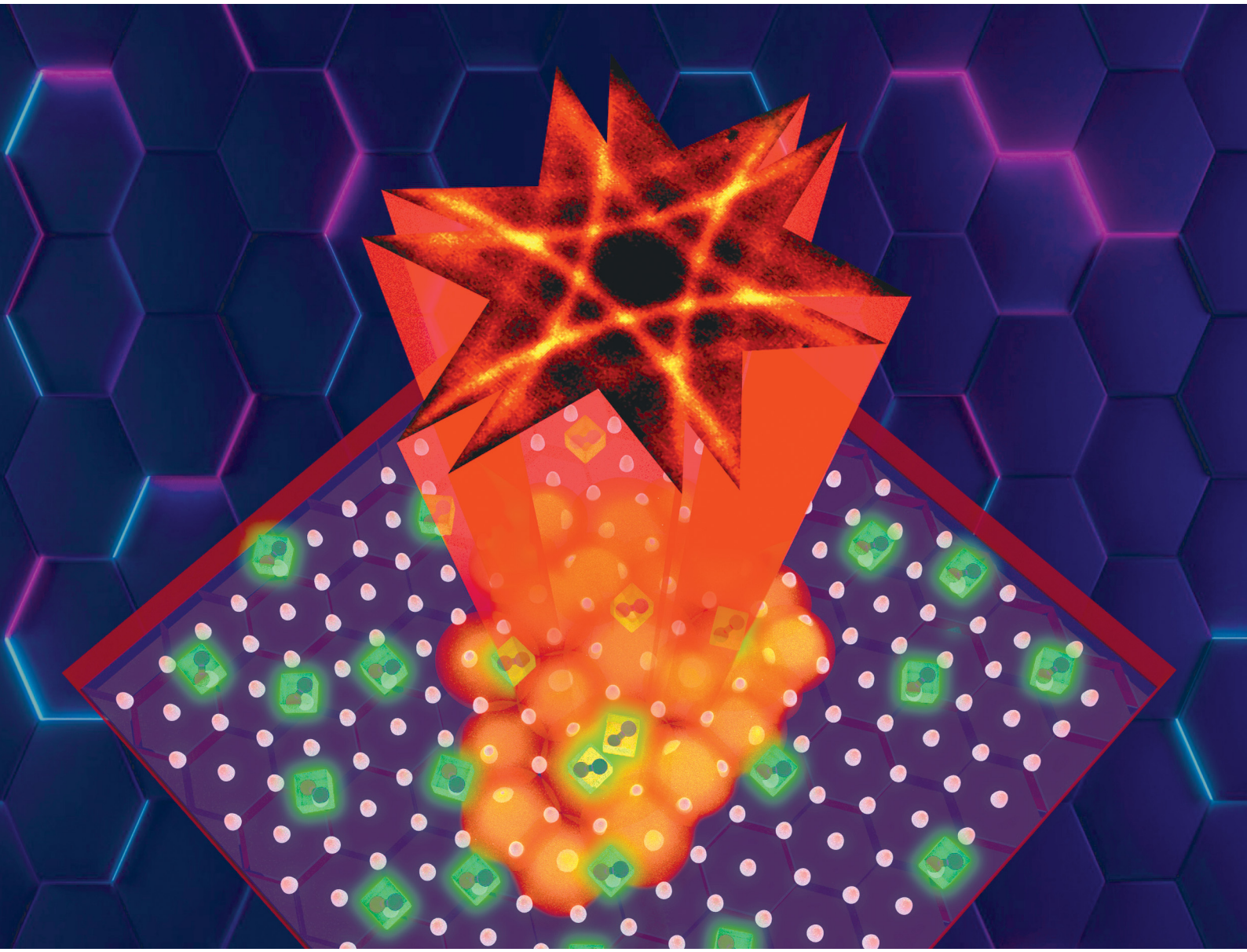

ISSN 2050-7526

ROYAL SOCIETY OF CHEMISTRY

PAPER

Hugo A. Lara-García, Giuseppe Pirruccio *et al.*
Shaping and enhancing the photoluminescence of halide perovskite quantum dots with plasmonic lattices

Journal of Materials Chemistry C

ROYAL SOCIETY OF CHEMISTRY

PAPER

View Article Online
View Journal | View Issue

Cite this: J. Mater. Chem. C, 2022, 10, 3704

Shaping and enhancing the photoluminescence of halide perovskite quantum dots with plasmonic lattices†

Elizabeth Mendoza-Sandoval,[a] Germán Rodríguez-López,[b] Cesar L. Ordóñez-Romero,[a] David Ley,[a] Naser Qureshi,[c] Michal Urbánek,[d] Diego Solis-Ibarra,[b] Cecilia Noguez,[a] Hugo A. Lara-García *[a] and Giuseppe Pirruccio *[a]

Received 4th November 2021,
Accepted 17th January 2022

DOI: 10.1039/d1tc05331k

rsc.li/materials-c

Halide perovskite quantum dots (PeQDs) are characterized by a size-dependent emission spectrum and an intrinsic lack of preferential emission directions. Thus, new means for shaping the typical Lambertian angular profile of thin layers embedding such PeQDs are highly desirable for several photonics applications, including solid-state lighting devices. Here, we show that the photoluminescence pattern of PeQDs can be changed drastically by weakly coupling them to plasmonic lattices at emission wavelengths. The coupling to extended collective optical modes supported by the lattices converts the ensemble of incoherent randomly oriented emitters into a spatially coherent source of polarized light with a wavelength-dependent intensity enhancement of about one order of magnitude. The dispersive character of the narrow collective optical modes is key to achieving intensity enhancement of the entire perovskite emission spectrum, especially its tails, together with beaming into definite directions. Further, we optimize the thickness of the perovskite layer to realize simultaneous shaping of its emission by plasmonic lattices of different symmetries. This flexibility paves the way to designing advanced photonic architectures based on PeQDs for solid-state lighting applications requiring programmable emission patterns.

Introduction

Lighting is one of the primary energy-consuming sources in our daily life. Therefore, it is of utmost importance to keep developing new materials and technologies to streamline the energy used for this purpose. Recently, halide perovskites have emerged as one of the most promising materials for opto-electronic applications.[1] Specifically, their low cost, large light absorption, high carrier mobility, defect tolerance, efficient free charge-carrier generation, and high photoluminescence quantum yield (PLQY) make them excellent candidates for next-generation solid-state lighting (SSL) devices, like efficient and miniaturized LEDs.[2] SSL benefits from the combination of quasi-monochromatic light sources and properly selected quantum emitters. In a typical integration, a thin layer of phosphor material, dyes, or quantum dots is pumped by a blue LED or by a laser. In this way, a color spectrum ranging from white to bright colors can be obtained depending on the mixing between the transmitted blue light and the emitted one.

Perovskite quantum dots (PeQDs) can provide unit PLQY, good photostability, low Auger recombination rate (compared to CdSe, PbSe),[3] a well-defined emission peak and a tunable bandgap and emission wavelength.[4] PeQDs can be classified based on their chemical composition, size and shape. This variety comes with outstanding optical properties, which have determined the emergence of PeQDs as versatile photonic sources. Mie resonances have been used to shape the emission spectrum of relatively large nanoparticles.[5] Amplified spontaneous emission from nanometer-size crystals forming densely packed aggregates has been reported.[6] Lasing has been observed for large individual perovskite crystals with lateral size of hundreds of nanometers,[7] nanoplatelets,[8] and microdisks.[9,10] Moreover, perovskite nanowires, acting as Fabry–Perot waveguides, have been used to demonstrate large Rabi splitting and lasing as a consequence of the exciton–photon coupling.[11]

[a] Instituto de Física, Universidad Nacional Autónoma de México, Apartado Postal 20364, México City, 01000, Mexico. E-mail: pirruccio@fisica.unam.mx, hugo.lara@fisica.unam.mx
[b] Instituto de Investigaciones en Materiales, Universidad Autónoma de México, (UNAM), Coyoacán, 04510, Ciudad de México, Mexico
[c] Instituto de Ciencias Aplicadas y Tecnología, Universidad Nacional Autónoma de México, CU, Coyoacán, Ciudad de México 04510, Mexico
[d] CEITEC BUT, Brno University of Technology, Brno 61200, Czech Republic

† Electronic supplementary information (ESI) available. See DOI: 10.1039/d1tc05331k

In contrast to fluorescent dyes and phosphors, PeQDs exhibit narrow and tunable emission, which is well suited for applications where pure colors are required. In addition to this, some modern applications, such as display technologies, document authentication, and advertising, demand uniform colors over a wide range of viewing angles. For some applications, a Lambertian emitter of unpolarized light is the best choice. However, these characteristics are a severe limitation for devices that require a defined angular emission profile and light polarization. Indeed, highly directional beams are critical in stereoscopic displays,[12] holographic displays,[13] optical communication,[14,15] and integrated lasers.[16] To serve these applications, secondary optics are typically needed, which may be bulky, lossy or degrade the total system efficiency. A possible solution is nanostructuring the emitting material to form metasurfaces and lattices that present enhanced absorption and photoluminescence.[5,17,18] Although viable, a more straightforward way of achieving directional emission is to couple the thin light-emitting layer to a nanostructure possessing an angular-dependent optical response. For instance, perovskite continuous films have been used as active material in distributed feedback and vertical-cavity surface-emitting lasers,[19,20] as well as in combination with photonic crystals.[21] On the other hand, metallic structures may be advantageous thanks to their plasmonic response. For instance, hybrid systems composed of disordered plasmonic nanoparticles and PeQDs have been realized to improve light conversion to electron–hole pairs.[22,23]

A step forward in the light-management strategy leverages the emergent properties of plasmonic lattices, *i.e.*, ordered arrays of coupled metallic particles. When the lattice parameter of the array is comparable with the wavelength of the incident light, radiative coupling occurs between the localized surface plasmons of the individual metallic nanoparticles. This interaction is enhanced by in-plane diffracted orders that propagate grazing the lattice plane.[24] The resulting collective modes are known as Surface Lattice Resonances (SLRs) and are characterized by large spatial and temporal coherence.[25] Moreover, since the associated enhanced electromagnetic field extends over the lattice unit cell, SLRs are excellently suited for tailoring light–matter interaction over large volumes.[26–29] By overlapping the optical modes of the nanostructure with the photoluminescence spectrum of the quantum emitters, their emission properties no longer depend solely on the chemistry of the material, but can also be altered by the properties of the photonic structure.

Herein, we use aluminum plasmonic lattices of different symmetries to demonstrate enhanced directional and polarized emission from a thin layer of $CsPbBr_3$ cubic quantum dots dispersed in a polymer matrix. The ease of deposition and no need for functionalization make our emitting layer compatible with solution-based and scalable fabrication processes. Importantly, directionality is obtained even though the emitting layer consists of randomly oriented and distributed nanocrystals. We achieve this thanks to the diffraction condition of the SLRs, which ensures a strong angular and spectral dependence of the emission. Notably, the enhanced emission is robust against surface imperfections of the aluminum structures composing the lattice, which is advantageous for applications in which achieving high fabrication precision is challenging. Our results are the first demonstration of plasmonic lattices shaping and enhancing the photoluminescence of PeQDs; as such, they open the door to many other PeQDs and plasmonic lattices to further control, enhance and exploit the optical properties of these promising materials.

Experimental section

Synthesis

$CsPbBr_3$ nanocubes synthesis. In a typical hot-injection synthesis, 0.2 mmol of $PbBr_2$ (73.4 mg) and 5 ml of 1-octadecene were loaded in a 25 ml three-neck round bottom flask, the mixture was nitrogen purged at 120 °C for 1 hour, then 0.5 ml of oleylamine and 0.5 ml of oleic acid were injected into the reaction flask, the mixture was stirred until all $PbBr_2$ was completely dissolved. Then 0.2 ml of OLA-HBr at 80 °C and 0.5 ml of Cs-oleate at 100 °C were injected successively. Immediately after the last injection, the reaction was cooled down in an ice bath. Then, 5 ml of the crude solution was loaded in a centrifuge tube with 5 ml of acetone, and centrifugated at 7000 rpm for 20 min. After centrifugation, the supernatant solution was discarded, and the precipitate was dispersed in toluene. Further information can be found in the ESI.†

PMMA solution. Different concentrations of PMMA (MW 350 000) were dissolved in 10 ml of toluene with a molar PMMA : toluene ratio of 2.5 mg : 1.0 ml. The solution was heated at 60 °C and stirred for a couple of hours until all the PMMA was dissolved.

Thin film. 30 mg of the $CsPbBr_3$ suspension were added to the PMMA solution. The perovskites were deposited by spin coating at 2000 rpm for 1 min. Afterward, the thin film was dried at 80 °C in a hotplate for 10 min.

Nanofabrication

Plasmonic lattices made of ordered arrays of aluminum nanocylinders were fabricated by electron beam lithography followed by reactive ion etching (see ESI†). Aluminum is chosen as the preferred material to enhance light–matter interaction in the green part of the visible spectrum, *i.e.*, where the PeQDs emission peaks. The diameter and height of the nanocylinders equal to 80 nm and 150 nm, respectively. We designed two Bravais lattices with square and triangular symmetry having lattice parameters equal to 340 nm and 375 nm, respectively. Fig. 1 shows SEM images of the plasmonic lattices fabricated on a common glass substrate. On top of them a thin layer of PMMA doped with $CsPbBr_3$ quantum dots was deposited. Both layer thickness and PeQDs concentration were systematically varied to achieve directional enhancement from the two lattices and the best extraction light, simultaneously. The optimal layer thickness was found to be around 350 nm. This value is a trade-off that provides an overall good performance of the two lattices.

Characterization

The crystal structure and the morphology were studied by transmission electron microscopy (TEM) in a JEM 2010 F

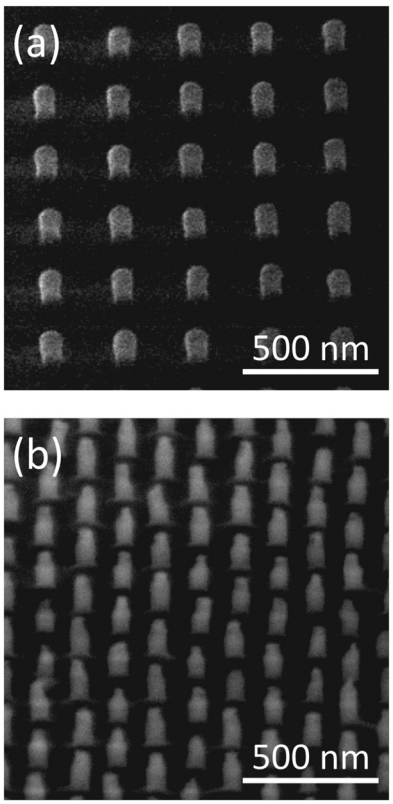

Fig. 1 SEM images of the (a) square and (b) triangular plasmonic lattices fabricated on a glass substrate.

FasTem analytical electron microscope. Microstructures of the thin films were studied by scanning electron microscopy (SEM). Backscattering electron images were obtained using a JEOL JMS-7800F Schottky Field Emission Scanning Electron Microscope.

The optical properties were studied by UV-vis diffuse reflectance spectra (DRS) in a UV-vis spectrophotometer (Shimadzu 2600) equipped with an integration sphere (ISR 2600) in the interval of wavelengths ranging from 400 to 700 nm and using $BaSO_4$ as a reference blank. The emission spectra of the sintered pellets were measured in a spectrometer (Edinburgh F900, Edinburgh Instruments, Livingston, UK).

Results

Since the very first report of the synthesis of $CsPbBr_3$ nanocrystals,[30] several attempts have been made to improve the synthesis method. This is the case for the synthesis reported by Dutta *et al.*[31] in which $CsPbBr_3$ nanocrystals size-tunable in a wide window were prepared using preformed alkylammonium bromide salt as a reagent to control the dimensions without varying the reaction temperature or changing the ligands. In the present report, PeQDs were fabricated by following the procedure described by Dutta *et al.*[31] The crystal structure was characterized by HRTEM by using Fourier analysis. Fig. 2 shows the HRTEM images and the FFT analysis. The distance of 0.29 nm could be indexed to the (220) crystal plane

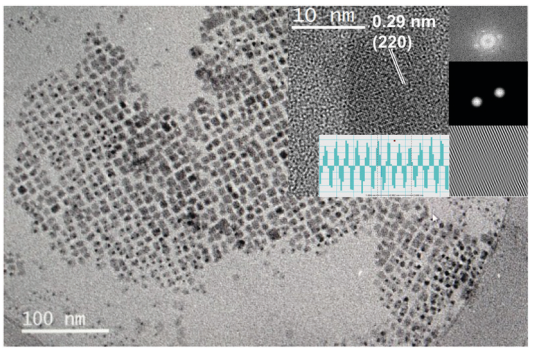

Fig. 2 TEM image and HRTEM with corresponding FFT pattern of PeQDs.

of the orthorhombic $CsPbBr_3$ phase (see insets), which is in good agreement with the work of Dutta *et al.*[31] where the orthorhombic phase is reported as the most stable one. A typical cubic morphology was observed with sizes between 4 and 11 nm with an average of 7.5 nm and a standard deviation of 1.6 nm (see Fig. 3 inset). Although the improvement reported with this synthesis method is the homogeneity of the particle size, we obtained a heterogeneous distribution. The heterogeneity of the size of the nanocrystals in the PeQDs can be attributed to two variables: (1) acid–base balance. The use of oleil amine-HBr reported in the synthesis technique used may have significant effects on the acid–base balance, affecting the size distribution of the nanocrystals.[32] (2) The use of acetone as an antisolvent contributes to the precipitation of smaller nanocrystals which has an impact in the emission. A comparative study about the effect of the antisolvent (methanol, 1-butanol, acetonitrile, acetone, methyl acetate, and ethyl acetate)[33] used in the purification of $CsPbBr_3$ shows that using acetone results in the widest full-width at half-maximum (FWHM) and the lowest photoluminescence quantum yield (PLQY), among all the antisolvent used. If a homogeneous distribution is desirable, the best antisolvent is methanol. Methanol is not soluble with ODE and, as a result, only precipitates a small portion of the largest nanocrystals in the sample, effectively resulting in size-selective precipitation.

We texturally characterized the thin layers using AFM and SEM. Fig. S1 and S2 (ESI†) show the images of the layer

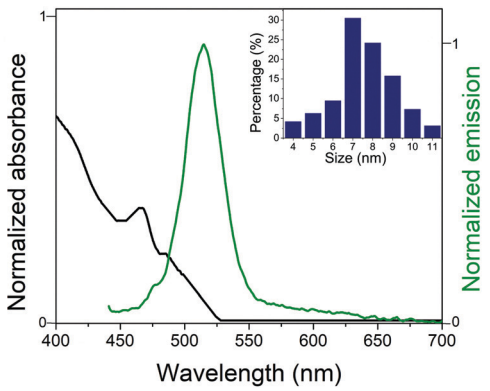

Fig. 3 Absorption and corresponding PL spectra of the $CsPbBr_3$ thin film and particle size (inset) measured by TEM.

deposited at 2000 rpm. Although the PMMA–$CsPbBr_3$ solution was stirred for several hours, it is evident that the layer is not completely homogeneous and is composed of cumulus of different sizes, being the biggest of around 1 μm. Besides, the thickness of the layer is an important feature that must be studied deeper. We found that at thickness higher than 400 nm the optical properties of our system (plasmonic lattice and PeQDs) were obscured by strong Fabry–Perot modes within the PeQDs layer. Therefore, in the experiments shown in the following, we kept the layer thickness below this value. The thickness was controlled by the PMMA concentration and the spin coater speed; we found that with a molar PMMA : toluene ratio of 2.5 mg : 1.0 ml, the thickness was lower than 500 nm. Fig. S2 (ESI†) shows a 3D image of one of the biggest cumulus. Although the cumulus' area was around 1 μm^2, the height was only 36 nm, which is convenient because the contribution to the total thickness of the layer is minimal.

The optical properties of the layer were studied by UV-Vis and photoluminescence spectroscopy. The PL emission peak is centered at 520 nm and has a full-width at half-maximum (FWHM) of 30 nm. The Gaussian shape and the FWHM of the emission peak are related to the heterogeneous $CsPbBr_3$ particle sizes and the cumulus formed in the thin layer leading to inhomogeneous broadening (see inset of Fig. 3). The emission wavelength can be determined by the size of the PeQDs and is tuned in a wide range of the visible spectrum when the particle size is homogeneous and below the Bohr exciton diameter,[31] which has been reported to be 7.0 nm for $CsPbBr_3$.[34,35] It is accepted that particles with size below this value present strong quantum confinement. Therefore, we associate the absorption peak around 480 nm with the strong quantum confinement of the particles with size below the Bohr diameter, which cause a Stokes shift of around 40 nm. Finally, most PeQDs typically have a large overlap between their absorption and photoluminescence spectra, leading to reabsorption losses.[36] The considerable Stokes shift of around 40 nm helps limiting reabsorption and improves the internal quantum efficiency. The PLQY in the PeQDs solution was 60% which is similar to the PQLY found by Zhang *et al.* when acetone is used as antisolvent.[33] On the other hand, the thin layer drops to 25%. The decay can be associated with the heterogenous distribution of the PeQDs into the thin film.

Aluminum is particularly well-suited to design systems with optical resonances in the green region of the spectrum, besides representing a low-cost alternative to the commonly used noble metals. The optical response of the individual nanocylinder has been simulated with the finite element method using COMSOL Multiphysics. In Fig. S6 and S7 of the ESI† we show the scattering and absorption cross-section spectrum, which exhibit a well-defined peak with a quadrupolar-like charge distribution, and a corresponding scattered electric field. We also plot the total electric field intensity at the resonance wavelength along two relevant symmetry planes. Once the nanocylinders are arranged in a lattice, diffractive orders are

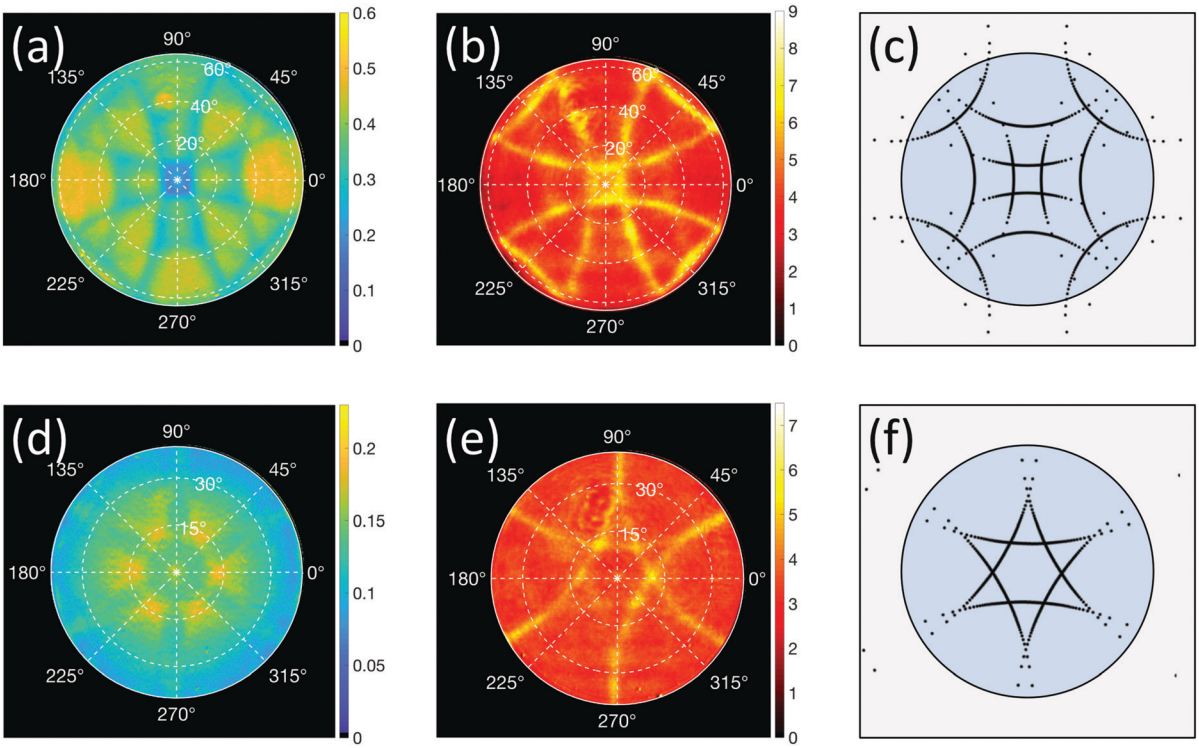

Fig. 4 Top (bottom) row relates to the square (triangular) plasmonic lattice and a wavelength of 520 nm. Reflectance [(a) and (d)] and PL enhancement [(b and e)] as a function of the azimuthal and elevation angles. (c and f) First order Rayleigh Anomalies calculated with effective refractive indices of 1.4 or 1. In all figures the circle indicates the maximum elevation angle measured.

excited coupling the individual resonant nanocylinders (see Fig. S8–S12 of the ESI†). The chosen lattice parameters ensure excitation of the SLRs in the green region of the visible spectrum, thus allowing the coupling to the PeQDs emission. This effect is illustrated in Fig. 4, where measurements of the unpolarized reflectance and PL enhancement (PLE) from the same diffraction-limited spot are compared utilizing Fourier microscopy (see ESI† for details on the experimental optical set-up). The PLE is obtained by normalizing the PL measurements with respect to the Lambertian emission from the same layer without the plasmonic lattice (see Fig. S3 in the ESI†). Even though we observed the presence of cumulus in the PeQDs layer, we emphasize that the overall homogeneity achieved in the layer was in general sufficient to conduct our PL and reflectance experiments in a reproducible and illumination-point independent manner.

The upper and lower rows refer to the square and triangular lattice, respectively. These measurements are performed by imaging on an sCMOS camera the back focal plane of the microscope objective used to illuminate and collect the reflected or emitted light from the sample. This means that reflectance and PLE are collected as a function of the elevation and azimuthal angles, (θ, φ), measured with respect to the normal of the sample surface. For reflectance, shown in Fig. 4(a and d), the sample is illuminated by a halogen lamp, while for PLE, displayed in Fig. 4(b and e), a 473 nm laser is used. For all cases, a bandpass filter centered at 520 nm with a FWHM of 10 nm selects the wavelength range around the maximum of the PeQDs emission spectrum (see Optical measurements in the ESI†).

For both lattices, well-defined regions of reduced reflection are observed, whose patterns reveal the symmetry of the corresponding unit cell. Such features are consistent with the zones of enhanced PL, which increases by a factor as high as 8. The narrow PLE angular width is comparable for the two lattices and makes the PeQDs a highly directional light source. This small PL divergence and its associated enhancement are explained in terms of the excitation of SLRs, hybrid plasmonic–photonic modes arising from the diffractive coupling between the localized resonances of the individual nanocylinders. For this reason, SLRs dispersion closely follows the Rayleigh anomalies (RAs), *i.e.*, in-plane diffracted orders grazing to the lattices. The black dashed curves plotted in Fig. 4(c and f) denote the RAs for the two types of lattices. These are calculated by enforcing the conservation of the parallel component of the wavevector:

$$\vec{k}_{\text{out},\parallel} = \vec{k}_{\text{in},\parallel} + \vec{G}(m_1, m_2), \quad (1)$$

where $\vec{k}_{\text{out},\parallel}$ and $\vec{k}_{\text{in},\parallel}$ depend on (θ, φ), and $\vec{G}(m_1, m_2) = \frac{2\pi}{a}$ (m_1, m_2) is the reciprocal lattice vector of the array where m_1 and m_2 the order of diffraction in the lattice plane, and a the lattice parameter. For a specific wavelength, the incident and diffracted wavevectors read:

$$\vec{k}_{\text{in},\parallel} = \frac{2\pi}{\lambda}\sin(\theta)(\cos(\varphi), \sin(\varphi)), \quad (2)$$

and

$$\vec{k}_{\text{out},\parallel} = \frac{2\pi}{\lambda} n_{\text{eff}}(\cos(\varphi), \sin(\varphi)). \quad (3)$$

By substituting the above expressions in eqn (1), taking the norm of the right- and left-hand side and rearranging the terms, the RAs in the (θ, φ)-plane are obtained. The effective refractive index of the system along the in-plane diffracted beams, n_{eff}, is used to describe the wave propagation within the emitting layer and at the air–PMMA interface. It takes values of either 1.4 or 1.1, found by adjusting the diffraction pattern to the optical measurements, with only a small dependence on the type of lattice. The stronger features observed in the reflectance correspond to the former case, meaning that the SLRs responsible for the stronger PLE are those whose field overlaps with the emitters. Interestingly, a moderate variation of the PLE value can be appreciated along the enhancement regions. Maximum PLE is found at the crossing points of RAs due to the interference between SLRs propagating in different directions within the PeQDs layer.

The spectral overlap between SLRs and the PeQDs emission occurs in narrow angular ranges. Nevertheless, since the mode dispersion extends over a broad wavelength range, we expect different wavelengths to be beamed into different and well-defined directions. To study the enhanced directional emission for an extended wavelength range, we first need to characterize the SLR dispersion relation. The latter can be extracted from the reflectance measurement as a function of the incident angle, θ, and wavelength. To do this, we image the reflected light from the sample onto the slit of a spectrograph coupled to an sCMOS camera and we project the measurement in p- or s-polarization.

Fig. 5(a) displays the s-polarized reflectance as a function of the incident wavelength and angle for the square lattice. The two main sharp dispersive features correspond to the excitation of SLRs associated with ($\pm$1, 0) diffracted orders propagating within the PeQDs layer. These are described by an effective refractive index of 1.4 (white curves). The SLRs excited between 500 nm and 550 nm at larger angles are associated with the ($\pm$1, 0) diffracted orders propagating close to the air–PMMA interface and thus are described by a refractive index of 1.05 (black curves). Although the dispersion of both pairs of SLRs overlaps with the whole PeQDs emission spectrum and in the reflectance measurements no substantial intensity difference is observed between them, only the former pair contributes strongly to the PLE (see Fig. 4). This is because the associated electric field is better confined to the emitting layer, as the associated n_{eff} indicates. In the ESI† we present the finite element method simulation of the reflectance, extinction and near electric field intensity for the square and triangular lattices. We obtain that the main SLR band is dipolar for both the square and triangular lattice. We also calculated the reflectance for different PeQDs layer thicknesses.

By applying the same optical technique to the PL instead of the reflection, the polarized PLE as a function of the emitted angle and wavelength can be imaged. This is shown in Fig. 5(b)

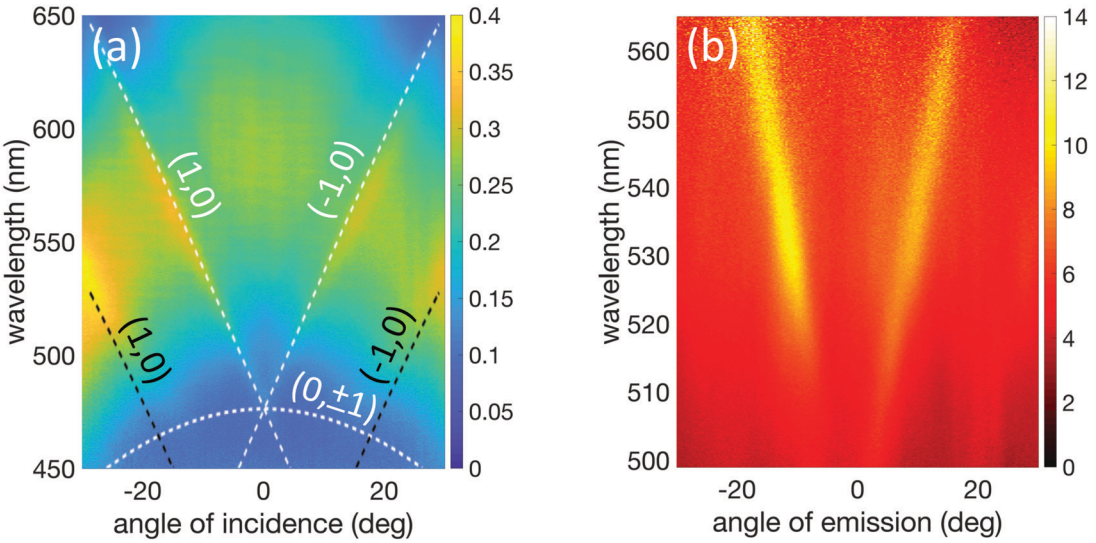

Fig. 5 Reflectance (a) and PLE (b) as a function of wavelength and angle of incidence and emission, respectively, for the square plasmonic lattice. The dashed curves correspond to Rayleigh anomalies. White and black curves correspond to a refractive index of 1.4 and 1.05, respectively.

for the s-polarization. A clear correspondence between the SLRs dispersion and the enhanced emission bands is found. The slight intensity asymmetry between these two bands is attributed to a minor optical misalignment. The PLE value for 520 nm agrees well with what is observed in Fig. 4. We highlight that the entire PL spectrum is enhanced and, in particular, the long-wavelength tail associated with larger PeQDs exhibits the highest PLE value (see Fig. S4 in the ESI†). Therefore, coupling a layer of randomly distributed PeQDs to the dispersive lattice modes allows taking advantage of the whole size distribution of the sample. The wavelength-dependence of the PLE value is due to the strength of the SLR at each emission wavelength. From Fig. 5(a) we see that the SLR is better excited at wavelengths longer than the peak one, which provides high emission intensity from the otherwise weak tails. Importantly, the PL modified by the coupling to the plasmonic lattices becomes polarized, even though the nanocrystals are randomly oriented within the layer. This characteristic is entirely determined by the polarization properties of the optical modes to which the emitters are coupled. Specifically, the near electric field of each SLR mode presents an involved polarization state. The QDs decay in presence of these SLRs. When the QDs emission is coupled to an SLR, it inherits the polarization state of the SLR mode to which it is coupled. Therefore the emission gets polarized.

Finally, we notice that the collective modes observed in reflectance do not participate significantly at the pump wavelength. Therefore, from Fig. 4 and 5, we deduce that the measured PLE mainly results from the emission enhancement, while pump enhancement plays a marginal role. The emission enhancement originates from the spectral overlap between the SLRs sustained by the plasmonic lattice and the PeQDs emission band. The angularly narrow PL features are explained by the SLR's enhanced spatial coherence that provides an efficient additional path for the out-coupling of the emitted light to free-space radiation. The remarkable observed PLE and directionality belong to the phenomenology of the weak coupling between the PeQDs emission and the lattice optical modes. Similar considerations can be made for the triangular lattice, although for this case a small contribution from pump enhancement can be expected (see Fig. S5 in the ESI†). This latter derives from the near-electric field intensity enhancement at the position of the PeQDs, which consequently increases their excitation efficiency. By leveraging it, the PLE from the PeQDs layer can be further increased. This can be accomplished by engineering the dispersion of the optical modes at the pump wavelength for instance by choosing a different polymer.[28] Also, using a high numerical aperture microscope objective to illuminate the sample facilitates the resonant coupling of the pump light in the emitting layer.

As a final remark, we briefly comment on the differences of using the triangular lattice with respect to the square one. Although the coupling mechanism is common to the two lattices and the enhancement and angular linewidth of the modified emission are comparable between the two lattices (see Fig. 4), the exact shaping of the emission spectrum and polarization depends on the details of the near-field of each SLR mode, which in turn may be sensitive to the symmetry of the near electric field.

Conclusions

We have shown a strong modification of the emission properties of PeQDs by coupling them to plasmonic lattices. Our implementation leverages the enhanced spatial and temporal coherence typical of the collective optical modes supported by the lattices, which results in efficient beam shaping. Specifically, we generate low divergent emitted beams of polarized light, which are angularly and spectrally tunable

through the geometrical parameters of the lattice, such as its symmetry and lattice parameter. We stress that the beaming effect is not significantly affected by defects of the single nanoparticles because it mainly depends on the long-range order of the lattice. Importantly, we demonstrated simultaneous coupling of the fabricated quantum dot layer to lattices with different symmetries. Since our approach can be adapted to any PeQDs, we envisage that our strategy will have a broad impact in the research field of perovskites for solid-state lighting. Our strategy is helpful to construct complex photonic architectures and hierarchically combined nanostructures that might influence the development of next-generation photonic devices.

Conflicts of interest

There are no conflicts to declare.

Acknowledgements

G. P. was supported by UNAM-PAPIIT IN114920, IN104522 and IN107319 and by Consejo Nacional de Ciencia y Tecnología 1564464 and 1098652. H. A. L.-G. thanks the support of UNAM-PAPIIT IA103621. C. L. O.-R. was supported by UNAM-PAPIIT IG100521. CzechNanoLab project LM2018110 funded by MEYS CR is gratefully acknowledged for the financial support of the sample fabrication at CEITEC Nano Research Infrastructure. G. R.-L. and D. S.-I. acknowledge the support of CONACYT's CB-A1-S-8729 and PAPIIT IN216020. The authors thank A. Gómez-Cortés and S. Tehuacanero-Cuapa for technical support.

References

1 K. Hong, Q. Van Le, S. Y. Kim and H. W. Jang, *J. Mater. Chem. C*, 2018, **6**, 2189–2209.
2 Z. K. Tan, R. S. Moghaddam, M. L. Lai, P. Docampo, R. Higler, F. Deschler, M. Price, A. Sadhanala, L. M. Pazos, D. Credgington, F. Hanusch, T. Bein, H. J. Snaith and R. H. Friend, *Nat. Nanotechnol.*, 2014, **9**, 687–692.
3 Y. Li, X. Luo, T. Ding, X. Lu and K. Wu, *Angew. Chem., Int. Ed.*, 2020, **59**, 14292–14295.
4 D. Chen and X. Chen, *J. Mater. Chem. C*, 2019, **7**, 1413–1446.
5 A. S. Berestennikov, P. M. Voroshilov, S. V. Makarov and Y. S. Kivshar, *Appl. Phys. Rev.*, 2019, **6**, 031307.
6 S. Yakunin, L. Protesescu, F. Krieg, M. I. Bodnarchuk, G. Nedelcu, M. Humer, G. De Luca, M. Fiebig, W. Heiss and M. V. Kovalenko, *Nat. Commun.*, 2015, **6**, 8056.
7 E. Tiguntseva, K. Koshelev, A. Furasova, P. Tonkaev, V. Mikhailovskii, E. V. Ushakova, D. G. Baranov, T. Shegai, A. A. Zakhidov, Y. Kivshar and S. V. Makarov, *ACS Nano*, 2020, **14**, 8149–8156.
8 Q. Zhang, R. Su, X. Liu, J. Xing, T. C. Sum and Q. Xiong, *Adv. Funct. Mater.*, 2016, **26**, 6238–6245.
9 Q. Liao, K. Hu, H. Zhang, X. Wang, J. Yao and H. Fu, *Adv. Mater.*, 2015, **27**, 3405–3410.
10 K. Wang, W. Sun, J. Li, Z. Gu, S. Xiao and Q. Song, *ACS Photonics*, 2016, **3**, 1125–1130.
11 W. Du, S. Zhang, J. Shi, J. Chen, Z. Wu, Y. Mi, Z. Liu, Y. Li, X. Sui, R. Wang, X. Qiu, T. Wu, Y. Xiao, Q. Zhang and X. Liu, *ACS Photonics*, 2018, **5**, 2051–2059.
12 D. Fattal, Z. Peng, T. Tran, S. Vo, M. Fiorentino, J. Brug and R. G. Beausoleil, *Nature*, 2013, **495**, 348–351.
13 S. Tay, P. A. Blanche, R. Voorakaranam, A. V. Tunç, W. Lin, S. Rokutanda, T. Gu, D. Flores, P. Wang, G. Li, P. St Hilaire, J. Thomas, R. A. Norwood, M. Yamamoto and N. Peyghambarian, *Nature*, 2008, **451**, 694–698.
14 H. Elgala, R. Mesleh and H. Haas, *IEEE Commun. Mag.*, 2011, **49**, 56–62.
15 S. K. Lim, K. G. Ruling, I. Kim and S. Il Jang, *IEEE Commun. Mag.*, 2013, **51**, 42–48.
16 A. S. D. Sandanayaka, T. Matsushima, F. Bencheikh, S. Terakawa, W. J. Potscavage, C. Qin, T. Fujihara, K. Goushi, J. C. Ribierre and C. Adachi, *Appl. Phys. Express*, 2019, **12**, 061010.
17 Q. Fan, G. V. Biesold-McGee, J. Ma, Q. Xu, S. Pan, J. Peng and Z. Lin, *Angew. Chem., Int. Ed.*, 2020, **59**, 1030–1046.
18 W. Liu, H. Zhou and G. Chen, *Cryst. Growth Des.*, 2020, **20**, 2803–2816.
19 N. Pourdavoud, T. Haeger, A. Mayer, P. J. Cegielski, A. L. Giesecke, R. Heiderhoff, S. Olthof, S. Zaefferer, I. Shutsko, A. Henkel, D. Becker-Koch, M. Stein, M. Cehovski, O. Charfi, H. H. Johannes, D. Rogalla, M. C. Lemme, M. Koch, Y. Vaynzof, K. Meerholz, W. Kowalsky, H. C. Scheer, P. Görrn and T. Riedl, *Adv. Mater.*, 2019, **31**, 1903717.
20 X. Fu, Y. Mehta, Y. A. Chen, L. Lei, L. Zhu, N. Barange, Q. Dong, S. Yin, J. Mendes, S. He, R. Gogusetti, C. H. Chang and F. So, *Adv. Mater.*, 2021, **33**, 1–10.
21 G. L. Whitworth, J. R. Harwell, D. N. Miller, G. J. Hedley, W. Zhang, H. J. Snaith, G. A. Turnbull and I. D. W. Samuel, *Opt. Express*, 2016, **24**, 23677.
22 S. Carretero-Palacios, A. Jiménez-Solano and H. Míguez, *ACS Energy Lett.*, 2016, **1**, 323–331.
23 Z. Lu, X. Pan, Y. Ma, Y. Li, L. Zheng, D. Zhang, Q. Xu, Z. Chen, S. Wang, B. Qu, F. Liu, Y. Huang, L. Xiao and Q. Gong, *RSC Adv.*, 2015, **5**, 11175–11179.
24 A. H. Schokker and A. F. Koenderink, *Phys. Rev. B: Condens. Matter Mater. Phys.*, 2014, **90**, 1–10.
25 V. G. Kravets, A. V. Kabashin, W. L. Barnes and A. N. Grigorenko, *Chem. Rev.*, 2018, **118**, 5912–5951.
26 W. Wang, M. Ramezani, A. I. Väkeväinen, P. Törmä, J. G. Rivas and T. W. Odom, *Mater. Today*, 2018, **21**, 303–314.
27 S. Murai, M. A. Verschuuren, G. Lozano, G. Pirruccio, S. R. K. Rodriguez and J. G. Rivas, *Opt. Express*, 2013, **21**, 4250.
28 G. Pirruccio, M. Ramezani, S. R. K. Rodriguez and J. G. Rivas,, *Phys. Rev. Lett.*, 2016, **116**, 1–6.
29 J. Guan, R. Li, X. G. Juarez, A. D. Sample, Y. Wang, G. C. Schatz and T. W. Odom, *Adv. Mater.*, 2021, 2103262.
30 L. Protesescu, S. Yakunin, M. I. Bodnarchuk, F. Krieg, R. Caputo, C. H. Hendon, R. X. Yang, A. Walsh and M. V. Kovalenko, *Nano Lett.*, 2015, **15**, 3692–3696.
31 A. Dutta, S. K. Dutta, S. Das Adhikari and N. Pradhan, *ACS Energy Lett.*, 2018, **3**, 329–334.

32 G. Almeida, L. Goldoni, Q. Akkerman, Z. Dang, A. H. Khan, S. Marras, I. Moreels and L. Manna,, *ACS Nano*, 2018, **12**, 1704–1711.
33 Y. Zhang, T. D. Siegler, C. J. Thomas, M. K. Abney, T. Shah, A. De Gorostiza, R. M. Greene and B. A. Korgel, *Chem. Mater.*, 2020, **32**, 5410–5423.
34 O. H. C. Cheng, T. Qiao, M. Sheldon and D. H. Son, *Nanoscale*, 2020, **12**, 13113–13118.
35 A. Shinde, R. Gahlaut and S. Mahamuni, *J. Phys. Chem. C*, 2017, **121**, 14872–14878.
36 H. Wu, Y. Zhang, M. Lu, W. Liu, J. Xu and W. W. Yu, *J. Nanopart. Res.*, 2016, **18**, 1–8.